Applied Surface Science 507 (2020) 145083

Contents lists available at ScienceDirect

Applied Surface Science

journal homepage: www.elsevier.com/locate/apsusc

Full Length Article

A study of heating rate effect on the photocatalytic performances of ZnO powders prepared by sol-gel route: Their kinetic and thermodynamic studies

Selim Demirci[a,b,*], Tuncay Dikici[c], Mehmet Masum Tünçay[a], Nusret Kaya[d]

[a] Marmara University, Department of Metallurgical and Materials Engineering, Kadikoy, 34722 Istanbul, Turkey
[b] Marmara University, Institute of Pure and Applied Sciences, Kadikoy, 34722 Istanbul, Turkey
[c] Dokuz Eylul University, Torbalı Vocational School, Welding Technology Department, Torbalı, 35860 Izmir, Turkey
[d] Katip Çelebi University, Central Research Laboratories Application and Research Center, 35620 Çiğli, Izmir, Turkey

ARTICLE INFO

Keywords:
Sol-gel method
Heating rate
Particle
Thermodynamic properties
Photocatalytic activity

ABSTRACT

In this work, ZnO particles were fabricated by sol-gel method at different heating rate at 500 °C for 2 h. The ZnO powders were analysed by X-ray diffraction (XRD), scanning electron microscopy (SEM), Raman spectroscopy, X-ray photoelectron spectroscopy (XPS), UV–vis spectroscopy and photoluminescence, respectively. The effect of heating rate on photocatalytic activities of ZnO particles was evaluated by degradation of methylene blue (MB). The non-isothermal kinetics and thermodynamic properties were also estimated. The XRD results showed that ZnO had hexagonal wurtzite structure. The different heating rate didn't influence the surface morphology of ZnO powders. It was observed that the heating rate had a profound effect on reduction of band gap and photocatalytic performances. The band gap of the ZnO particles varied from 3.10 to 3.17. The ZnO sample prepared at 1 °C/min exhibited the highest photocatalytic activity. Its relative photocatalytic degradation rate and kinetic constant were 92.7% and $1.069 \times 10^{-2}\,min^{-1}$, respectively. The results might be ascribed to low bulk vacancies, high surface oxygen vacancies and narrow band gap energy. Also, ZnO photocatalysts showed good stability after four sequence tests. This study provides a new strategy to improve the photocatalytic performances of ZnO photocatalyst for the degradation of organic contaminant.

1. Introduction

Cleaning and removing of environmental pollution by photocatalysis process has been becoming more important area because of the rapid industrial growth in the worldwide [1–3]. As photocatalysts are exposed to light, the electrons liberate from valance band to conduction band because of higher energy of photons than band gap energy and form electron and hole pairs. These obtained pairs contact with the adsorbed oxygen molecules and water molecules on the surface in order to form superoxide radicals ($^{\cdot}O_2^-$) and hydroxyl radicals ($^{\cdot}OH$) after reaction. These produced reactive radicals interact with the adsorbed pollutants resulting in their degradation [4]. Photocatalysis process has gained essential attention for pollutant treatment. Because, it is an inexpensive and convenient method that can totally decompose organic pollutants into small molecules (H_2O, CO_2, etc.) [5,6]. There have been different kind of nanostructured semiconductor materials such as ZnO, TiO_2, Fe_2O_3, CeO_2, SnO_2, and WO_3, etc. which have been used for photocatalytic degradation in order to get rid of environmental pollution in water and wastewater treatment [7,8]. Amongst those nanostructured semiconductor materials, zinc oxide (ZnO) has been widely used because of its versatile, nontoxic, inexpensive, unique electronic and optical properties for application of photocatalytic process up to now [9,10]. ZnO has a wide direct band gap (3.37 eV) which generates electron–hole pairs under UV light or visible light irradiation and high electron binding energy of 60 meV at room temperature [11,12]. Many approaches have been reported in literature up to now such as thermal annealing [13], wet chemical [14], coprecipitation [15], spray pyrolysis [16], hydrothermal [17] and sol-gel [18] method etc. in order to produce ZnO structures with different form varying from nanoparticles, nanotubes, nanofibers nanorods, nanoribbons, nanosheets, nanocups, quantum dots, nanowires and thin films [19]. Among those methods, sol-gel has been becoming one of the most popular method because of its high controllability, simplicity, reproducibility and possibility to produce cheap materials [20,21]. The sol-gel method allows to fabrication of high purity and homogeneous oxides in different formation. So far, there have been numerous studies about ZnO nanostructured materials which have been used for photocatalytic degradation of organic pollutant prepared by sol-gel method

* Corresponding author at: Marmara University, Department of Metallurgical and Materials Engineering, Kadikoy, 34722 Istanbul, Turkey.
E-mail address: selim.demirci@marmara.edu.tr (S. Demirci).

https://doi.org/10.1016/j.apsusc.2019.145083
Received 30 October 2019; Received in revised form 12 December 2019; Accepted 14 December 2019
Available online 16 December 2019
0169-4332/

[22–24]. There are numerous studies and reports related to effect of parameters during sol preparation such as pH, molarity, temperature etc. The various preparation parameters involved in sol-gel method such as amount of water, solvent, pH, calcination temperature and holding time etc. have profound influences on morphological and structural change which consequently modify electrical, optical, dielectric and magnetic properties of ZnO final material [25,26]. In addition to that, the parameters during calcination or thermally annealing process of xerogel particles can also influence final properties. To the best of our knowledge, there are only two studies about impact of heating rate during the calcination or annealing process on ZnO material's properties. Gao et al. [27] synthesized Al-doped ZnO films by means of sol-gel method at different heating rate regime. The electrical and structural properties were investigated. The results showed that ZnO nanorod film was obtained by rapid heating rate. Furthermore, rapid heating rate improved the electrical conductivity of ZnO film. Lingling and coworkers [28] fabricated rod-like ZnO nanostructure via pyrolysis of zinc acetate in order to investigate how the heating rate and calcination affect photocatalytic performances of methyl orange (MO) and 4-nitrophenol. They claimed that the heating rate influenced the morphology, optical and photocatalytic activity. ZnO nanorod particles prepared at 1 °C/min heating rate had the best photocatalytic efficiency due to oxygen vacancies. In this work, we prepared xerogel powders in the same preparation sol condition and investigated how the heating rate regimes affect final properties of the xerogel powders during thermal annealing in the furnace. Our study is different from the two studies as mentioned above. Therefore, this study shows novelty in terms of preparation of ZnO particles with different heating rate regimes during thermal annealing process after obtaining xerogel powders by using sol-gel method and evaluation of photocatalytic degradation of MB solution. This paper reports effect of the different heating rate on material crystallinity, surface morphology, intrinsic electronic properties and photocatalytic degradation performances of ZnO particles prepared by sol-gel method. Moreover, thermodynamic kinetic calculation is investigated for production of ZnO particles. Structural, morphological, optical and photocatalytic degradation of methylene blue (MB) were scrutinized meticulously. The results showed that ZnO particles produced at 1 °C/min heating rate regime possessed the highest photocatalytic activity.

2. Experimental details

2.1. Materials and methods

Zinc nitrate hexahydrate ($Zn(NO_3)_2 6H_2O$, 99%, Aldrich Chemistry) was used as starting raw material in order to synthesize ZnO particles. 59.488 g of Zinc nitrate hexahydrate was added to 300 ml absolute ethanol. The solution was stirred for 30 min in order to complete the hydrolysis process so as to obtain homogenous and transparent solution. After obtaining the transparent sol formation, 3 ml of glacial acetic acid and 0.1 mol of trietanolamin were added to solution as the chelating agent under vigorous stirring for 24 h to facilitate gel formation. The solution was aged one day for the gelation process. After gelation process, the gel form was dried at 120 °C for 5 h to obtain the xerogel structure. The xerogel powders were thermally annealed at 500 °C for 2 h with different heating rate regime. The heating rate regimes for fabrication of ZnO powders were 1 °C/min, 5 °C/min, 10 °C/min, 20 °C/min and ∞ °C/min, respectively.

2.2. Materials characterization

Thermogravimetric (TGA) and differential thermogravimetry analysis (DTA) were performed by TA TGA-SDT Q600 machine under air atmosphere. X-ray diffraction analysis was carried out by using Rigaku ULTIMA 3–Rint 2200/PC instrument. This instrument works with voltage and current settings of 40 kV and 36 mA, respectively, and uses Cu-K_a radiation (1.54185 Å). The morphologies of the ZnO powders were observed through a scanning electron microscopy (SEM, Carl Zeiss 300 VP). Elemental composition and surface chemistry of ZnO powders were examined by XPS (Thermo-Scientific) with monochromatic Al-K_a (1486.7 eV) X-ray source and a beam size of 400 nm diameter. Confocal Raman analysis were made by trademark Renishaw Invia Raman microscope. The laser was 532 nm wavelength with 2400 l/mm gratings. 7.3 mW laser power was applied to on to the samples. Optical measurement was measured via UV–Vis spectrophotometer machine with diffused reflectance apparatus (PG Instruments T92 + UV–VIS Spectrophotometer) in the wavelength range of 300–800 nm. Photoluminescence (PL) emission spectra were performed by using a FLS920 spectrofluorometer. Decay time was measured with a time correlated single photon counting (TCSPC) system that was from Edinburgh Instruments (UK). The instrument was equipped with a standard xenon lamp and a microsecond flash lamp for steady-state and lifetime measurements, respectively.

2.3. Photocatalytic measurement

The photocatalytic performances of ZnO particles were tested in a homemade reactor by using methylene blue (MB) solution under UV light source (Osram, UltraVitalux E27, 300 W). Light intensity is 190 mW/cm^2. The initial concentration of MB solution was 10^{-5} M (pH = 8). The distance between the lamp and the beakers was kept at 30 cm for all specimens. During the whole reaction, 3 ml of the MB aqueous solution from each beaker was extracted at certain time intervals in order to measure the absorption spectra of MB. The absorption of the MB solutions based on the characteristic peak at 664 nm was conducted and analyzed by a spectrophotometer (Shimadzu, UV-1240). Prior to photocatalytic study, ZnO samples were immersed in 30 ml of MB solution and then stirred to vigorously in the dark condition for 1 h to reach adsorption–desorption equilibrium between the ZnO particles and methylene blue. The concentration of MB solution was tested for every 30 min for all ZnO structures. Furthermore, the mineralization of MB dye was analyzed by total organic carbon analyzer (TOC) (Shimadzu Model: TOC-VLPH TOC analyzer). During the experiment, the photocatalytic degradation efficiency and mineralization performance (η) was calculated by using the following formula:

$$\eta = \left(\frac{C_0 - C}{C_0}\right) \times 100 \quad (1)$$

where η = MB % or % TOC, C_o and C are the concentrations of η at the initial time and given time t.

3. Results and discussion

3.1. TG analysis, non-isothermal transformation kinetics and thermodynamic studies

Thermogravimetric analysis (TGA) of the prepared ZnO precursors at different heating rate are employed in order to investigate thermodynamic studies. TGA plots of the prepared ZnO precursors were depicted in Fig. 1. As can be seen in Fig. 1, two weight loss stages were observed. In the first stage, the weight loss was approximately % 30 which might ascribe to volatilization of solvents such as ethanol and moisture, thermal decomposition of Zn based oxalate complex and their transform to Zn hydroxide form between 200 °C and 300 °C. The temperature range originates from the different heating rate. It was very obvious that the curve of the TGA of the samples shifted towards higher temperature values when the heating rate increased. In the second stage, the weight loss was almost 5% which should be due to the decomposition of the organic compound and conversion of Zn hydroxide to ZnO form at around 400 °C. No weight change was observed at higher temperature particularly after 500 °C [29,30]. Furthermore, non-

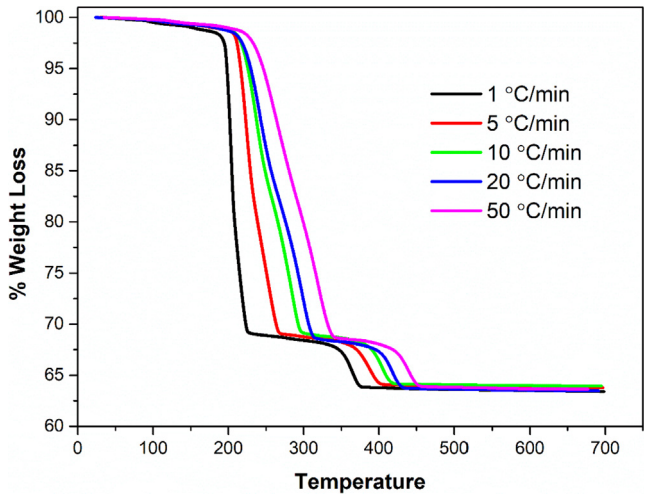

Fig. 1. TGA curves of the prepared ZnO xerogel powders at different heating rate under air atmosphere.

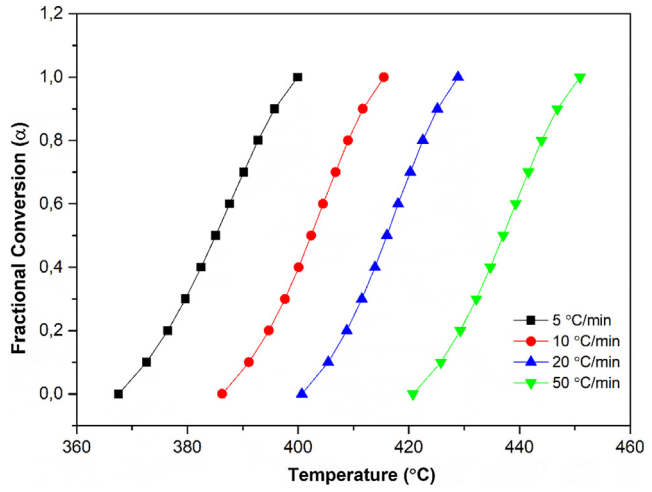

Fig. 2. The plot of fractional conversion (α) versus temperature (T).

isothermal kinetics and thermodynamic values were calculated. The second stage was taken into consideration in order to determine the non-isothermal kinetics and thermodynamic studies. General speaking, there are two different ways to determine kinetics and thermodynamic values. These are model-free and model-fitting for non-isothermal techniques. Nowadays, the model-free techniques have attracted much attention because of application of easier and quicker calculation of kinetic parameters such as pre-exponential factor (A) and the activation energy (E_a) [31]. The well-known model-free techniques are Flynn–-Wall–Ozawa (FWO) (Eq. (2)), Kissinger-Akahira-Sunose (KAS) (Eq. (3)) and Starink (Eq. (4)) technique which are described as following equations, respectively [32–34].

$$log\beta = \log\left(\frac{AE_a}{Rg(\alpha)}\right) - 2.315 - 0.4567\frac{E_a}{RT} \quad (2)$$

$$\mathrm{Ln}\left(\frac{\beta}{T^2}\right) = ln\frac{AR}{E_a g(\alpha)} - \frac{E_a}{RT} \quad (3)$$

$$\mathrm{Ln}\left(\frac{\beta}{T^{1.92}}\right) = C_{Starink} - 1.0008\frac{E_a}{RT} \quad (4)$$

A, β, R, E_a and g(α) are pre-exponential factor, heating rate, gas constant, activation energy and proper mechanism function, respectively. Firstly, fractional conversion (α) for different heating rate are required in order to estimate thermodynamic values and kinetic studies. Fig. 2

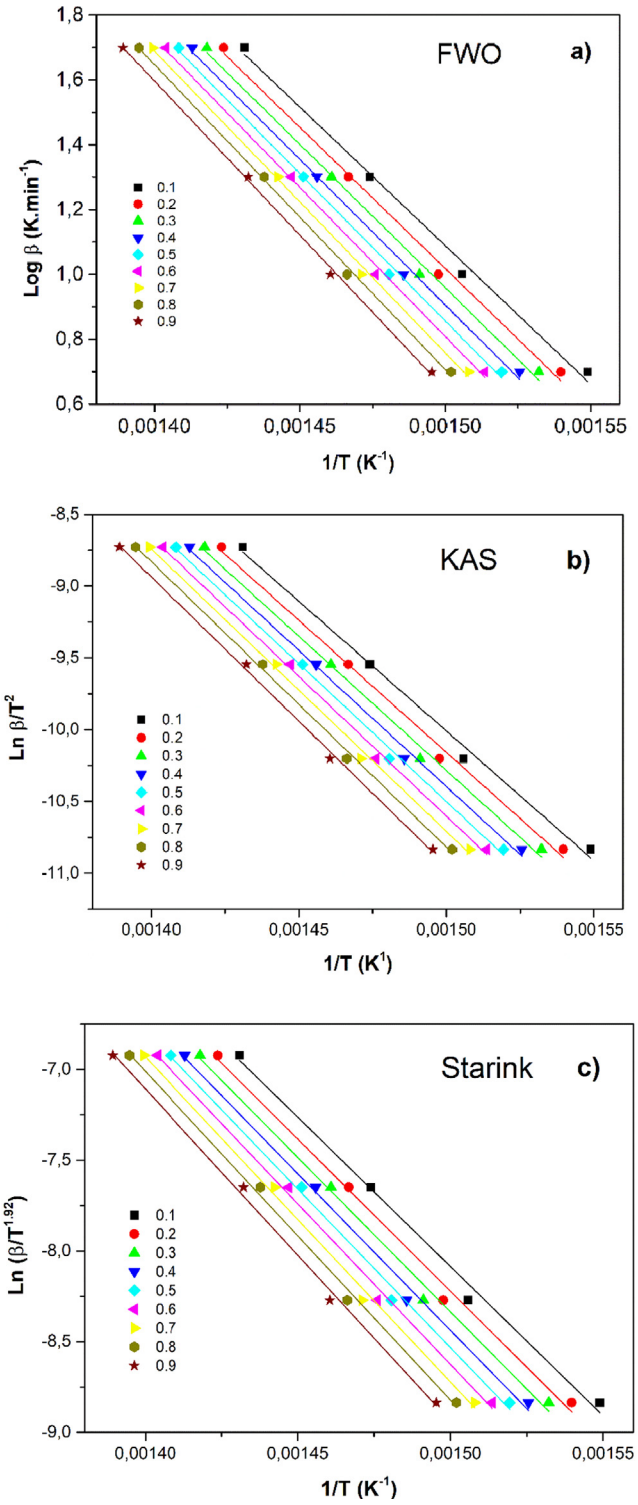

Fig. 3. The curves of the FWO (a), KAS (b) and Starink (c) model-free models for thermodynamic calculations.

illustrated the fractional conversion of ZnO precursor. After obtaining fractional conversion plot, the well-known model free techniques should be applied in order to assess thermodynamic and kinetic studies. The curves of FWO, KAS and Starink model-free techniques were shown in Fig. 3. The activation energy (E_a) for each model free techniques might be determined by using the slope of plots based on above mentioned equations. The calculated activation energy (E_a) values for each method were given in Table 1. According to Table 1, FWO method had

Table 1
Activation energies and pre-exponential factors based on FWO, KAS and Starink methods.

A	FWO		KAS		STARINK	
	Activation Energy (E_a) (kJ/mol)	LnA (s^{-1})	Activation Energy (E_a) (kJ/mol)	LnA (s^{-1})	Activation Energy (E_a) (kJ/mol)	LnA (s^{-1})
0.1	155.57	13.91	150.11	17.07	136.66	16.59
0.2	158.54	14.08	152.98	17.44	139.29	16.93
0.3	160.97	14.22	155.31	17.74	141.41	17.19
0.4	163.29	14.36	157.55	18.03	143.44	17.46
0.5	165.47	14.49	159.64	18.30	145.34	17.71
0.6	167.51	14.61	161.59	18.55	147.11	17.94
0.7	169.45	14.72	163.47	18.78	148.82	18.15
0.8	171.35	14.82	165.29	19.00	150.47	18.35
0.9	173.11	14.91	166.99	19.18	152.02	18.51
Average	**165.03**	**14.46**	**159.21**	**18.23**	**144.95**	**17.65**

Table 2
Thermodynamic parameters of ZnO powders.

B (°C/min)	ΔH (kJ/mol)	ΔG (kJ/mol)	ΔS (J/molK)	T_p (°C)
5	152.21	211.67	−0.118069311	230.5422
10	152.08	213.56	−0.118329592	246.5556
20	152.00	214.64	−0.118474976	255.7208
50	151.78	217.79	−0.118882864	282.3069
Average	152.02	214.42	−0.118439186	

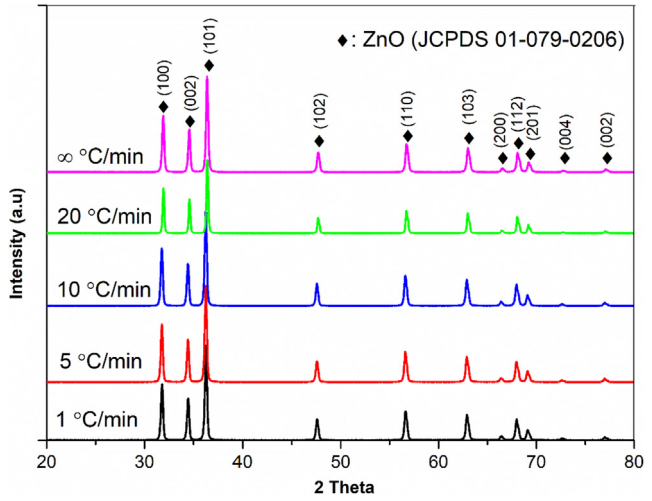

Fig. 4. X-ray diffraction (XRD) pattern of the ZnO powders prepared with different heating rate.

the highest the activation energy (E_a) values. The thermodynamic properties such as Gibbs free energy (ΔG), enthalpy (ΔH) and entropy (ΔS) were investigated according to the following equations [35].

$$LnA - \frac{E_a}{RT_p} = Ln\frac{kT_p}{h} - \frac{\Delta G}{RT_p} \quad (5)$$

$$\Delta H = E_a - RT_p \quad (6)$$

$$\Delta G = \Delta H - T_p\Delta S \quad (7)$$

where k and h represent the Boltzmann and Planck constant, respectively. T_p is the peak temperature. The calculated thermodynamic values were given in Table 2.

3.2. XRD analysis

XRD analysis was exploited to characterize phase and crystalline structure for the prepared ZnO nano-scale particles. Fig. 4 showed the XRD results of the analyzed ZnO particles. It could be said that the fabricated ZnO particles showed strong, sharp and intense diffraction peaks. It is noticeable to mention that having narrow, sharp and intense diffraction peaks is an indication of the existence of highly crystalline phases which means to the enhancement of crystallinity degree for the fabricated ZnO nano-scale particles. All the diffraction peaks were indexed to hexagonal wurtzite structure of ZnO (JCPDS 079–0206, $P6_3mc$). No other phases were detected. The diffraction peaks were observed at 2θ values of 31.76°, 34.42°, 36.29°, 47.62°, 56.68°, 62.93°, 66.46°, 67.99°, 69.13°, 72.58° and 77.62° with corresponding to (1 0 0), (0 0 2), (1 0 1), (1 0 2), (1 1 0), (1 0 3), (2 0 0), (1 1 2), (2 0 1), (0 0 4) and (0 0 2) miller indice planes, respectively. According to Fig. 4, the peak at 2θ = 36.29° with (1 0 1) miller indice plane had the highest intensity which is main peak for all the samples. Based on the diffraction spectrum of the prepared ZnO particles in Fig. 4, it is worthwhile to note that there was no remarkable change in terms of the intensity of produced ZnO particles when the heating rate was varying from 1 °C/min to ∞ °C/min. Moreover, the crystalline size mean of the prepared ZnO particles were calculating from main diffraction peak (1 0 1) by means of Deybe-Scherrer equation [36]. The equation is described by following equation; $D = \frac{k\lambda}{\beta cos\theta}$ where k is 0.94, λ is the X-ray wavelength, β is the peak width at half-maximum in radian and θ is the Bragg's angle. According to Deybe-Scherrer equation, the calculated crystalline size of the prepared ZnO particles were quite close to each other. There was slightly difference between the crystalline size which could be negligible. The crystalline size values of the produced ZnO particles were 6.97, 7.21, 7.13, 7.87 and 6.68 nm concerning the heating rate (1, 5, 1, 20 and ∞ °C/min), respectively.

3.3. Surface morphology

The surface morphologies of ZnO particles were characterized by SEM to explore shape and size of ZnO nanostructures. The SEM images shown in Fig. 5 revealed that ZnO samples had granular, spherical and round-like structures. The SEM figures indicated a homogeneous shape and size for ZnO particles. The SEM imaged showed the ZnO powders were well dispersed in the powder form. Also, the SEM images of ZnO samples demonsrated that the fabricated particles had high degree of agglomeration. Furthermore, the particle size of ZnO samples varied from 100 nm to 300 nm. The agglomeration might originate from higher energy of ZnO particles [37].

3.4. XPS analysis

The XPS measurement was carried out in order to scrutinize and gain chemical information and the oxidation states of the elements of ZnO powders. Fig. 6(a) displayed the XPS survey spectra of ZnO sample which was produced at 1 °C/min heating rate. It was obtained that the ZnO composed of Zn, O and C elements. The dominant peaks belonging

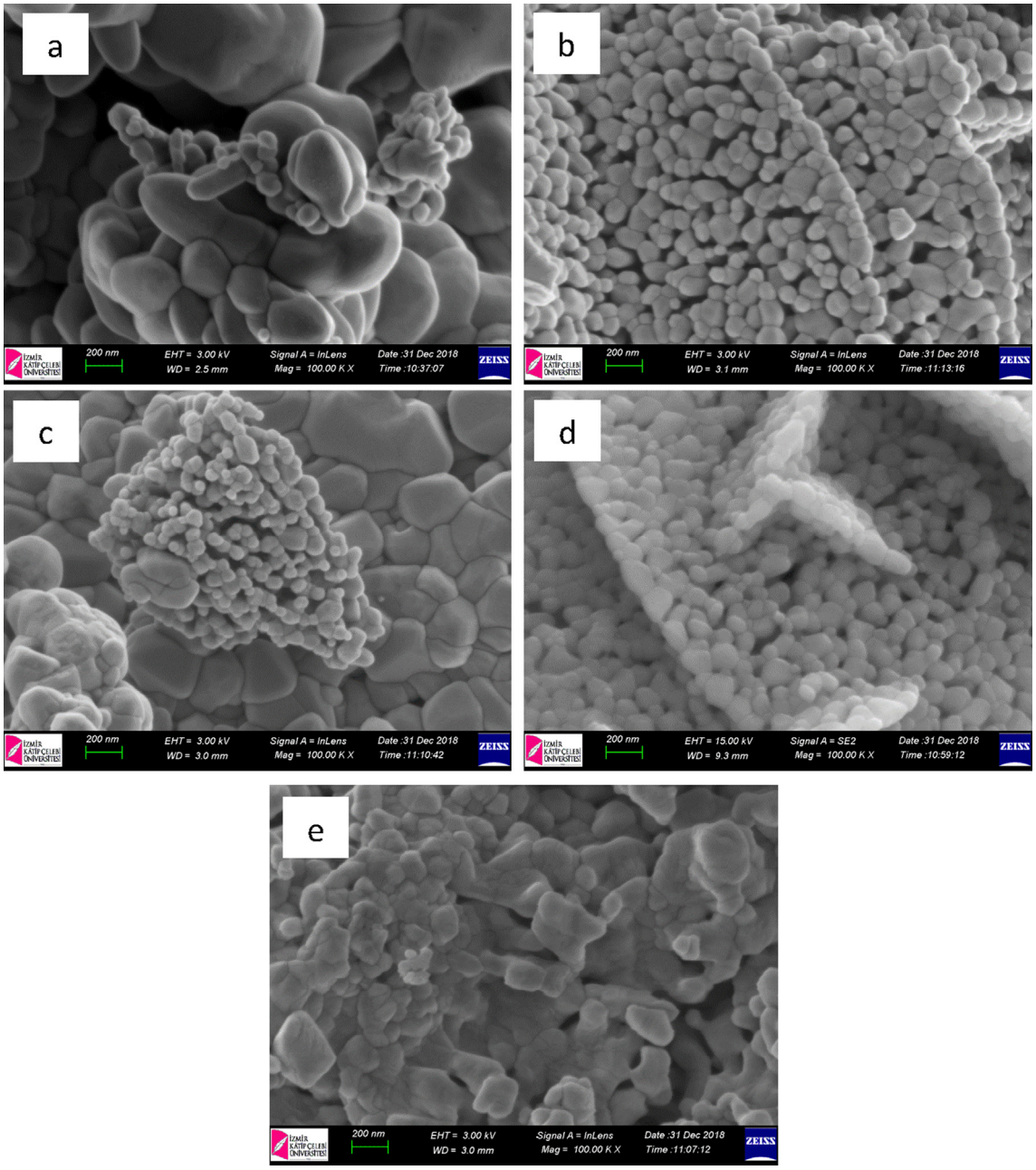

Fig. 5. SEM images of the ZnO powders annealed at 500 °C at different heating rate (a) 1 °C/min. (b) 5 °C/min. (c) 10 °C/min. (d) 20 °C/min. and (e) ∞ °C/min.

to Zn and O were clearly detected as could be seen in the Fig. 6(a). The existence of carbon is due to absorbed from the environment which is impossible to be removed from the surface. Furthermore, Fig. 6(b) and (c) exhibited the high resolution XPS scans over Zn 2p and O1s peak regions, respectively. As shown in Fig. 6(b), the binding energy peaks of Zn 2p3/2 and Zn 2p1/2 at 1022.38 eV and 1045.48 eV, respectively. The binding peaks at 1022.38 eV and 1045.48 eV might be ascribed to Zn-O bond which corresponds to Zn^{2+} in ZnO structure [38,39]. As can be seen in Fig. 6(c), the binding energy peak at 531.18 eV confirmed the existence of absorbed OH group on the ZnO surface [40,41].

3.5. Confocal Raman analysis

The confocal Raman spectra of ZnO particles prepared at different heating rates were given in Fig. 7. According to literature, perfect ZnO wurtzite crystal (space group of symmetry $P6_3mc$) group has six Raman active modes which can be defined $\Gamma_{opt} = A_1 + E_1 + 2E_2 + 2B_1$ where A_1 and E_1 are polar modes. B_1 and E_2 represent silent and nonpolar modes, respectively [42–44]. Special Raman modes were observed as can be seen in Fig. 7. Transversal acoustics (TA) and E_2^{low} modes were seen at 204 cm^{-1} in the spectrum which were related with Zn sublattice vibration of ZnO crystals. The Raman bands of ZnO particles at 333 cm^{-1} represented difference of two E_2 silent modes. Transversal optical (TO) of A_1 was observed at 334 cm^{-1} which was about polarity of Zn and O bonds. E_1 (TO) silent modes of ZnO particles seen at 412 cm^{-1}. E_2^{high} mode of ZnO particles was observed at 436 cm^{-1} which was attributed to oxygen atom vibration of ZnO crystal lattice. In other words, it is indication of crystallinity. [45]. Longitudinal acoustic (LA) mode was observed at 540 cm^{-1} which was ascribed to phonon–phonon interaction into the ZnO lattice. The other important Raman band was E_1(LO) mode seen at 581 cm^{-1} which was concerned with lattice defects and impurities of ZnO particles. The presence of high intensity E_1(LO) mode might be appointed to the oxygen deficiencies such as oxygen vacancies (V_O) [46]. TA and LO bands were

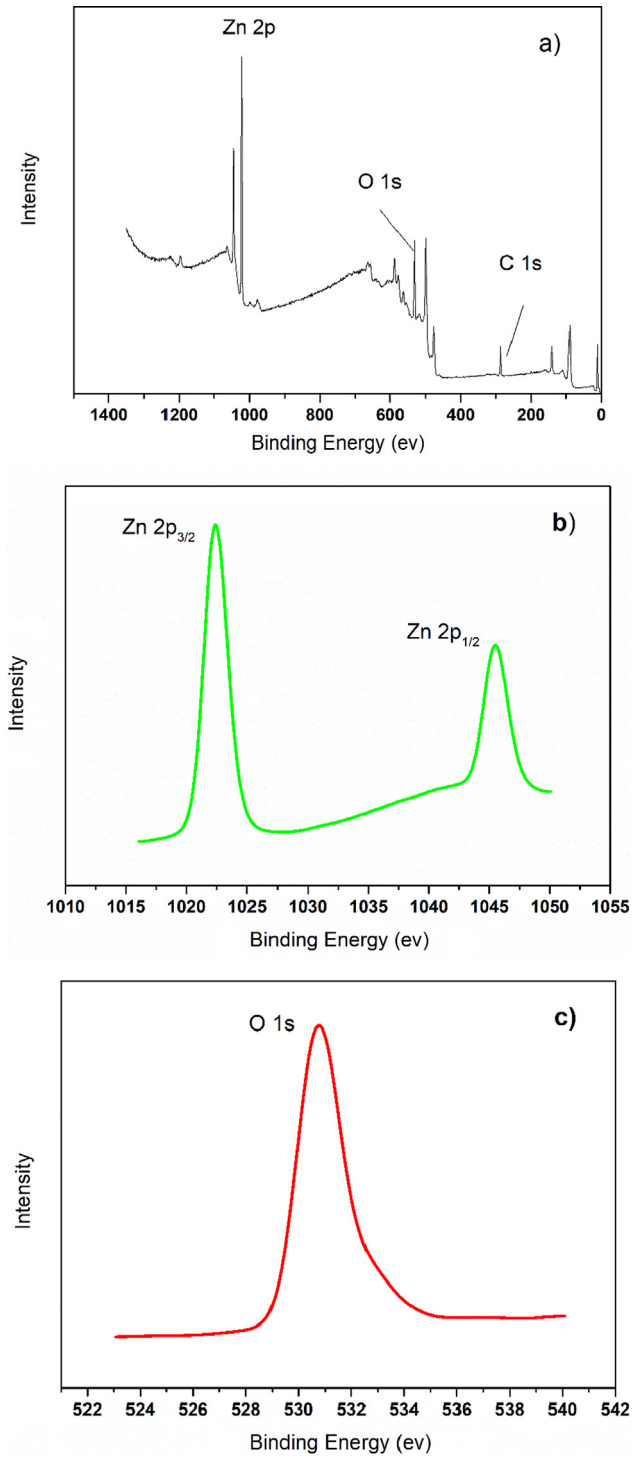

Fig. 6. XPS spectra of ZnO powders prepared at 1 °C/min heating rate: survey spectrum (a) and high-resolution spectra for Zn 2p (b) and O 1 s (c).

seen at 615 cm^{-1} [47]. According to Table 3, even though E_2^{high} mode Raman bands position did not change significantly with increasing heating rate ZnO powders but their intensity of the mode changed. Full width of high maximum (FWHM) values of ZnO particles of E_2^{high} mode decreased almost 3.2% for ZnO sample prepared at 20 °C/min heating rate. The decrease in FWHM of E_2^{high} mode represented for increasing disorder of oxygen atoms in ZnO particles lattice. Moreover, the heating rate also affected E_1(LO) mode position and FWHM of ZnO particles. E_1(LO) mode positions were almost same for ZnO samples prepared at 5, 10 and ∞ °C/min heating rates. The position of E_1(LO) mode

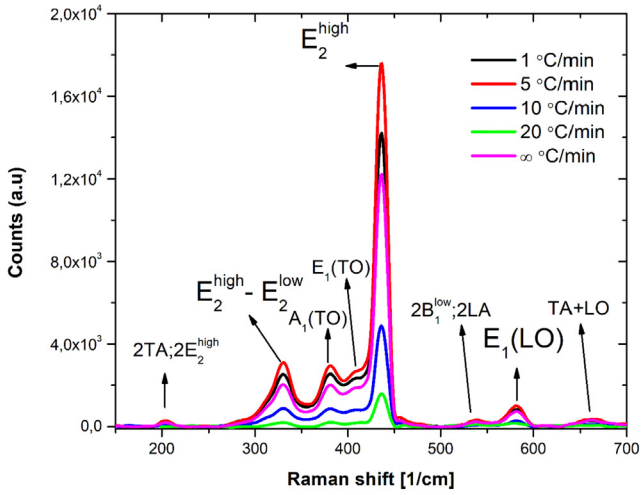

Fig. 7. Raman spectra of ZnO particles between 100 and 700 cm^{-1} which are annealed at 1 °C/min, 5 °C/min, 10 °C/min, 20 °C/min, and ∞ °C/min heating rate.

Table 3
Wavelength of E_2^{high}, E_1(LO) modes, FWHM and intensity ratio were given for ZnO particles.

Raman Band	1 °C/min	5 °C/min	10 °C/min	20 °C/min	∞ °C/min
E_2^{high}	436.16	436.14	436.09	436.21	436.07
FWHM (E_2^{high})	15.639	15.549	15.626	15.102	15.657
E_1(LO)	582.18	581.71	581.4	579.36	581.84
FWHM (E_1(LO))	20.862	21.317	18.589	34.974	21.962
$I - E_2^{high}/I - E_1$(LO)	16.95	17.45	16.98	9.64	16.55

changed ± 1 cm^{-1} when ZnO samples prepared at 1 and 20 °C/min heating rate were taken into consideration. The intensity of E_2^{high} and E_1(LO) modes were compared. ZnO particles prepared at 20 °C/min heating rate had the lowest I-E_2^{high}/I-E_1(LO) ratio. Scepanovic et al [47] explained that having lower intensity ratio of I-E_2^{high}/I-E_1(LO) was about oxygen atom defects amounts and increasing anisotropy in the ZnO crystal lattice. All Raman analysis results showed that the heating rate directly affected atomic orientation of ZnO crystal lattice. ZnO powders fabricated with a heating rate of 5 °C/min exhibited the highest ratio which means obtaining perfect crystal lattice and low zinc and oxygen atom vacancies in ZnO crystal. Hence, ZnO sample prepared at 5 °C/min heating rate could has high degree crystallinity based on Raman spectrum.

3.6. Optical properties

The reflectance spectra of the all ZnO samples were measured in the range of 300–800 nm, as shown in Fig. 8(a). The UV–Vis reflectance value was used to determine the optical band gap energy (E_g) of the prepared ZnO powders. The corresponding diffuse reflectance spectra of all samples was converted into the the Kubelka-Munk (K-M) function to estimate band gap energy by using the following equation [13,28]

$$F(R) = \frac{(1-R)^2}{2R} \quad (8)$$

where R and $F(R)$ are the reflectance and Kubelka-Munk function, respectively. The Kubelka-Munk (K-M) function was utilized to construct Tauc plot of $(F(R)h\nu)^{0.5}$ versus photon energy ($h\nu$), as shown in Fig. 8(b). E_g was calculated by extrapolating the linear part of the plot of $(F(R)h\nu)^{0.5}$ versus ($h\nu$) to the × axis. It was found in the Fig. 8(b) that the band gap energies of fabricated ZnO particles were estimated to vary between 3.10 and 3.17 eV. The ZnO sample prepared at 1 °C/min heating rate regime possessed the lowest band gap energy which was

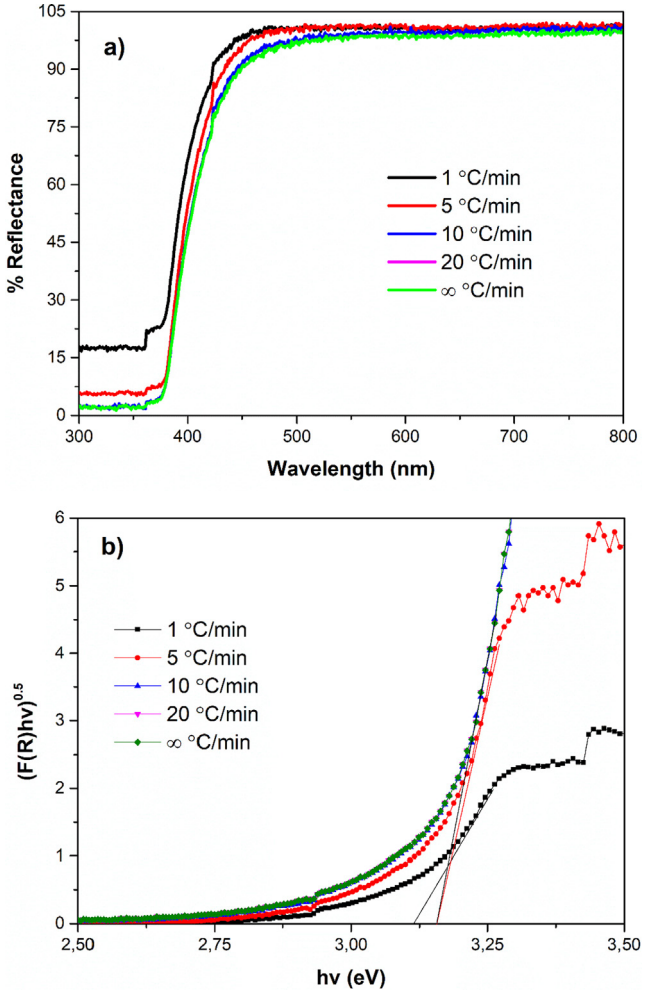

Fig. 8. Optical diffuse reflectance spectra (a) and energy band gap (b) of ZnO powders fabricated at different heating rate at 500 °C.

~3.10 eV. The highest band gap value was 3.17 eV which belonged to ZnO powders fabricated at ∞ °C/min heating rate regime. Other ones' band gap energies were found 3.15 eV. Having the lower band gap energy has a profound effect on enhancement of photocatalytic performances due to absorption ability of much light.

3.7. Photocatalytic performances

The photodegradation efficiency of ZnO particles was studied. The photocatalytic properties of the ZnO samples were given in Fig. 9. The absorbance spectrum of MB solution containing ZnO particles against time was given in Fig. 9(a). It can be deduced that the prepared solution was purified from MB organic dye with increasing time according to the absorbance spectrum of MB at 664 nm. Fig. 9(b) showed relative degradation of MB solution for ZnO powders prepared at different heating rate regime. Also, the photodegradation of MB solution without photocatalytic was given in order to compare and evaluate direct photolysis. It was observed that ZnO sample prepared at 1 °C/min heating regime exhibited the highest photodegradation performances which was 92.7% degradation efficiency. It can be understood that the ZnO sample prepared at 1 °C/min heating rate regime had the strongest and fastest photocatalytic activity. The ZnO sample fabricated at ∞ °C/min heating rate regime exhibited the lowest photodegradation efficiency. The degradation efficiency of the lowest one is 79.5%. Fig. 9(c) illustrated the percent of the degradation rate of MB in the form of bar chart in order to compare each other easily for ZnO structures. The photocatalytic kinetic study of the ZnO particles was also investigated in order to understand kinetic mechanism. As can be seen in Fig. 9(d), the photocatalytic degradation kinetic mechanism follows the pseudo-first order kinetic model which was defined as given below formula:

$$\ln(\frac{C_o}{C}) = kt \quad (9)$$

C_0 and C are the original concentration of MB and the corresponding concentration along with the exposure time (t), respectively and k is the degradation rate constant. The k values can be extracted from the linear shape of the data. The slope of the linear fittings represents the reaction rate constants (k) of the MB solution [48]. It was apparent in Fig. 9(d) that the ZnO particles fabricated at 1 °C/min heating rate regime possessed the biggest degradation rate constant (k) that was 1.069×10^{-2} min^{-1} value, whereas the ZnO powder synthesized at ∞ °C/min heating rate regime showed the lowest rate constant (k). The lowest rate constant was approximately 0.578×10^{-2} min^{-1}. Moreover, the photocatalytic degradation rate constant (k) tended to decrease when the heating rate regime increased. The aim of this study was to prepare photocatalysts able to achieve the total degradation of organic compounds, it was necessary to measure the real degree of mineralization of the MB dye. This degree can be evaluated on the basis of the total amount of organic carbon (TOC) remained in the solutions after the reactions were over. The % TOC of ZnO particles prepared at different heating rates was given in Table 4. According to the Table 4, mineralization performances of ZnO particles for 1 °C/min, 5 °C/min, 10 °C/min, 20 °C/min and ∞ °C/min heating rate regimes showed % 74.5, % 69.9, % 60.1, % 59.7, % 56.7, respectively after 210 min of UV irradiation. These results depicted that the photocatalytic activity of the prepared ZnO particles changed with heating rate regime. It can be considered that the distinct in the degradation efficiency might originate from various surface features, crystallinity and optical properties for ZnO structures. Firstly, the optical band gap energy is crucial to generate more charge carriers which involve the photocatalytic process. Having a low band gap energy stimulates the generation of more charge carriers as the materials are exposed to external energy. ZnO particles produced at 1 °C/min heating rate had the lowest band gap energy when the optical band gaps were considered and compared. Therefore, its photocatalytic performance should be better. Secondly, the distinct in photocatalytic performance of the fabricated ZnO particles should derive from surface oxygen defects. According to the Raman spectrum, ZnO samples prepared at 1 and 5 °C/min heating rates had higher intensity for E_1(LO) mode than that of other ones. The finding represented that ZnO samples prepared at 1 and 5 °C/min heating rate held much more surface oxygen defects which acted as charge carrier traps where charges easily move and react with adsorbed species without recombination of the photogenerated electrons and holes [49]. This is very important to improve the photocatalytic efficiency. In addition, the decrease in photocatalytic activity as an increase in heating rate could be attributed to bulk or native defects in ZnO crystal lattice. These bulk or native defects capture the photogenerated electrons/holes. These defects act as a recombination centers [46,50,51]. Photoluminescence and Raman analysis supported this results in this study. Emission intensity of ZnO samples rose with increasing heating rate when the photoluminescence analysis was analyzed. The rise could be assigned to boosting of bulk or native defects [52]. Therefore, ZnO particles prepared at 1 °C/min heating rate had the lowest defects which consequently showed better photocatalytic efficiency. E_2^{high} mode of ZnO particles observed at 436 cm^{-1} in Raman spectrum was related to totally about oxygen atom vibration of ZnO crystal lattice. In other words, it is an indicator of how perfect crystalline phase is formed. Augmentation of intensity of E_2^{high} mode depicts the existence of high crystalline degree materials. Hence, ZnO samples prepared at 1 and 5 °C/min heating rate could have high degree of crystallinity. They had the highest intensity of E_2^{high} mode in Raman spectrum. Having higher degree of crystallinity enhances the photocatalytic performance

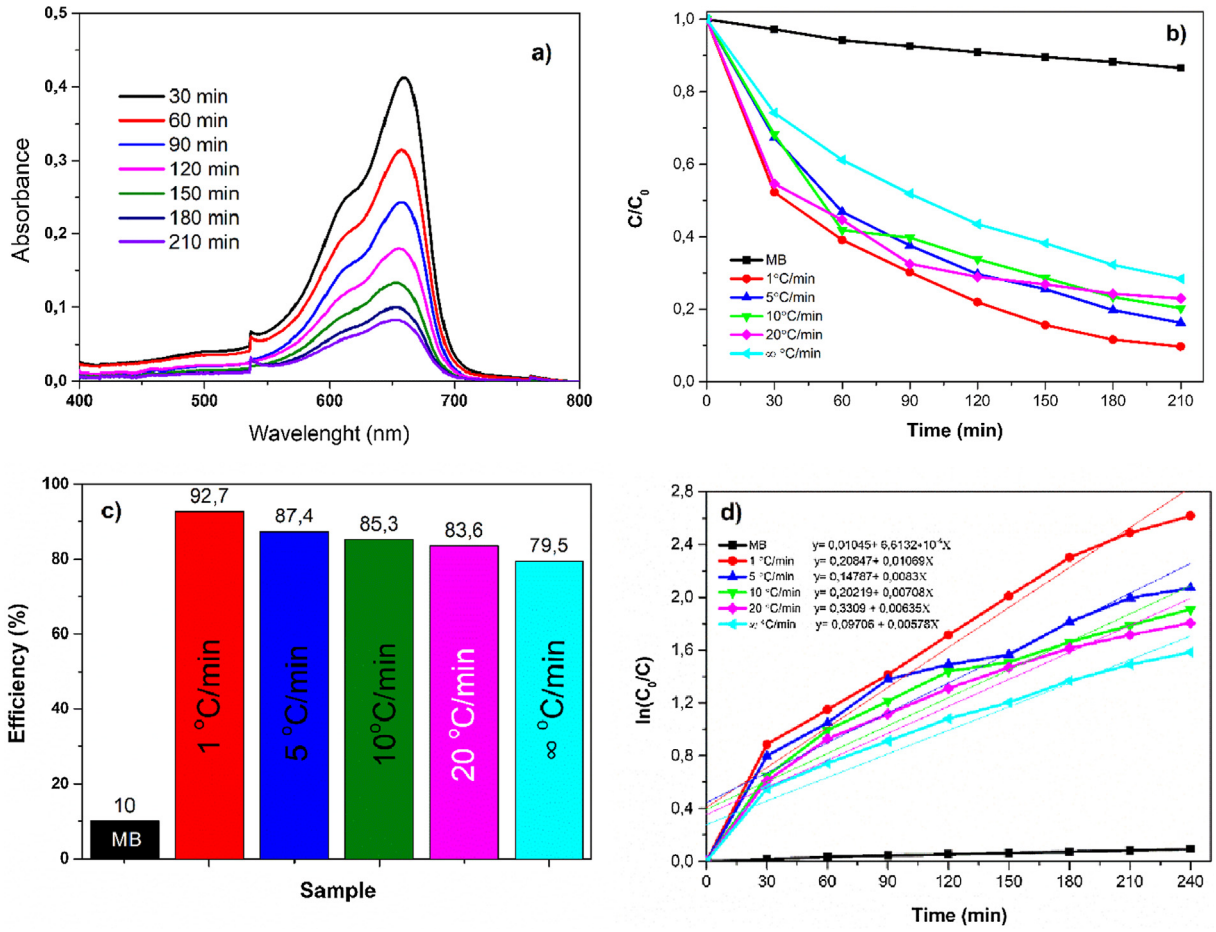

Fig. 9. (a) Absorbance spectrum of MB solution versus irradiation time, (b) relative concentration changes (C/C_0) of MB solutions, (c) photocatalytic degradation efficiency (η) of ZnO photocatalysts against irradiation time and (d) photocatalytic degradation kinetic constant of ZnO photocatalysts.

Table 4
% TOC removal under 210 min irradiation time.

Samples	TOC (mg/L)	% TOC Removal
MB Blank	120.2	0.248
ZnO (1 °C/min)	30.7	74.5
ZnO (5 °C/min)	36.2	69.9
ZnO (10 °C/min)	48.0	60.1
ZnO (20 °C/min)	48.5	59.7
ZnO (∞°C/min)	52.1	56.7

[53]. Within this framework, the highest photocatalytic efficiency for ZnO particles prepared at 1 °C/min heating rate might be ascribed to low band gap energy, higher degree of crystallinity and more surface oxygen vacancies. Furthermore, Mott-Shottky and EIS analysis were conducted in order to comprehend intrinsic electronic properties at the semiconductor/electrolyte interface region. The carrier densities(N_d) of ZnO particles fabricated at different heating rates might be calculated using following equation [13,54].

$$N_d = \frac{2}{q\varepsilon\varepsilon_0 A^2 slope} \quad (10)$$

in which q is the electron charge, ε is the dielectric constant (for ZnO, ε = 10), ε_0 is the permittivity of vacuum and A is area. The slope values for prepared ZnO particles can be obtained from Mott-Shottky plots in Fig. 10. The carrier densities (N_d) of ZnO particles for 1 °C/min, 5 °C/min, 10 °C/min, 20 °C/min and ∞ °C/min heating rate regimes were found to be 3.7×10^{22}, 1.85×10^{22}, 6.44×10^{21}, 2.4×10^{19} and 9.42×10^{16}, respectively. It is apparent that the carrier density findings support our photocatalytic performances. Because, the ZnO sample prepared at 1 °C/min heating rate had the highest carrier densities. Hence, the possibility of the photogenerated electron and hole pairs which involve in surface reaction with adsorbed species is higher than that of others which enhances photocatalytic activity. Also, the EIS spectra was given in Fig. 10(f). The smaller arc radius implies efficient carrier charge transfer at semiconductor/electrolyte interface. In other words, the resistance during the transfer becomes smaller [13]. In this context, the ZnO particles manufactured at 1 °C/min heating rate possessed the lowest arc radius and charge transfer resistance. The arc radius for ZnO particles soared with increasing heating rate regime. The comparison of our study with literature in terms of photocatalytic parameters was given in Table 5. According to the Table 5, our samples showed better photocatalytic activity as compared to literature. The photocatalytic reactions are conducted by three main active species: holes (h^+), superoxide radicals ($^{\cdot}O_2^-$), and hydroxyl radicals ($^{\cdot}OH$). The capture experiments were conducted to determine the active species generated during the photocatalytic process of ZnO particles including some scavengers. Ammonium oxalate (AO), ascorbic acid (AC), and isopropyl alcohol (IPA) were used as scavengers to capture holes (h^+), superoxide radicals ($^{\cdot}O_2^-$), and hydroxyl radicals ($^{\cdot}OH$), respectively [75,76]. The effects of scavengers on the MB degradation efficiency were shown in Fig. 11. The type of the photocatalytic mechanism was determined by the change in the relative concentration of MB by addition of scavengers into the photocatalytic system. Only 38.5% of the MB was degraded when ascorbic acid (AC) was added into the system as shown in Fig. 11. The degradation rate of MB was 39.7% in the presence of isopropyl alcohol (IPA). For the addition of Ammonium oxalate (AO), the photodegradation ability of MB was 72.2%. The

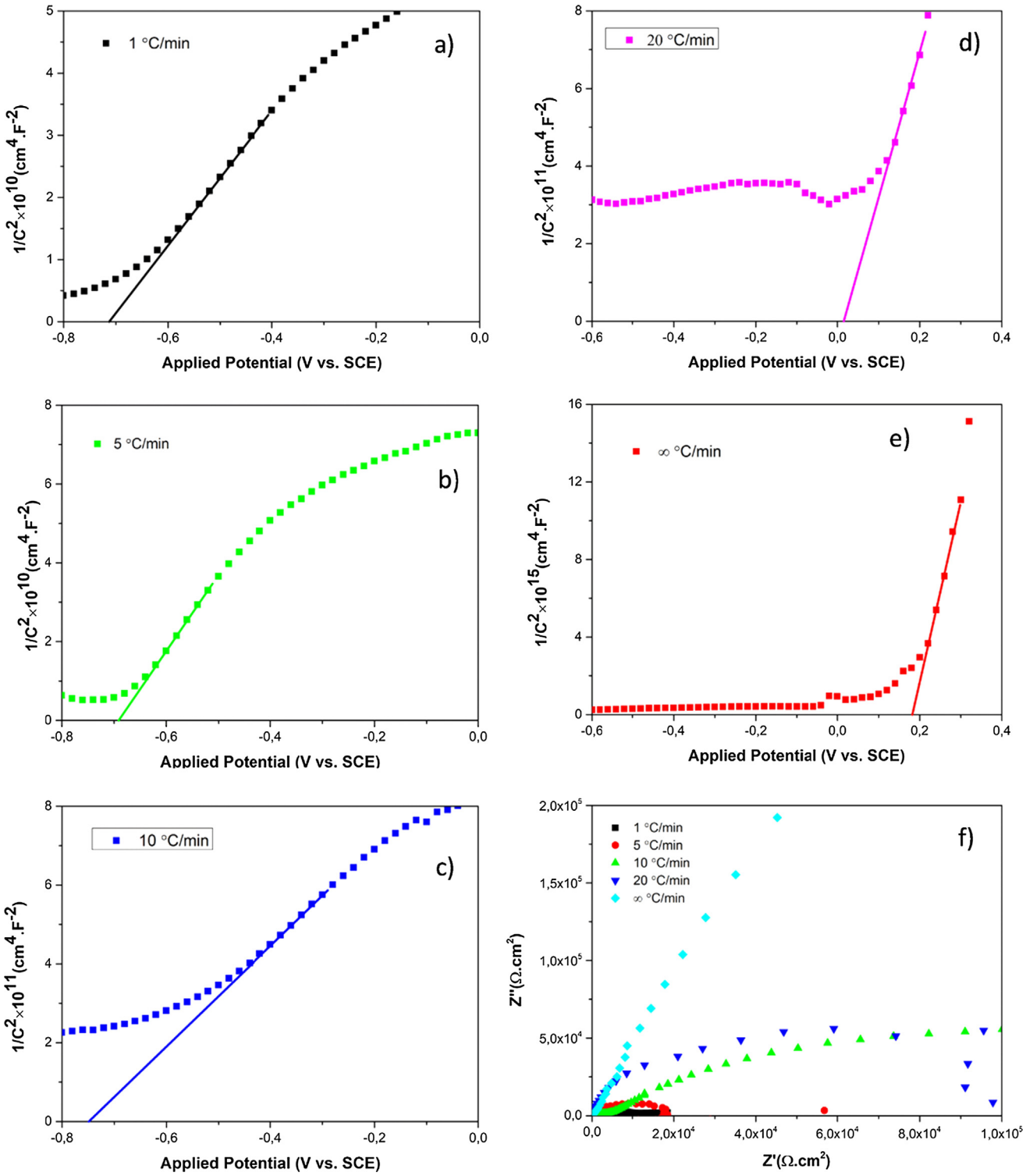

Fig. 10. Mott-Schottky curve of (a) 1 °C/min, (b) 5 °C/min, (c) 10 °C/min, (d) 20 °C/min, (e) ∞ °C/min and (f) EIS spectra of ZnO nano particles prepared at different heating rates.

degradation rate of the MB solution was obviously limited with loading of the active species into the photocatalytic system. The decrease is due to trapping of photogenerated radicals by scavengers. These results clearly indicated that the hydroxyl radicals (˙OH), and superoxide radicals ($\dot{O}_2^-$) played the important role in the photocatalytic process. Those active species were dominant for degradation process. The photocatalytic mechanism of MB solution using by ZnO particles could be described by the following equations

$$ZnO + h\nu \rightarrow ZnO\ (e^- + h^+) \quad (11)$$

$$ZnO\ (e^-) + O_2 \rightarrow ZnO + \dot{O}_2^- \quad (12)$$

$$ZnO\ (h^+) + OH^- \rightarrow ZnO + \dot{O}H \quad (13)$$

$$ZnO\ (h^+) + H_2O^- \rightarrow \dot{O}H + H^+ \quad (14)$$

$$Dye + (\dot{O}_2^- + \dot{O}H) \rightarrow Degradation\ Products \quad (15)$$

Table 5
The comparison of our study to the reported studies of the ZnO particles in terms of photocatalytic degradation performances.

Photocatalytic	Synthesis Method	Time (min)	Light Source	Photodegradation amount (%)	k_{app} (min^{-1})	Ref.
ZnO nanoparticles	Sol-gel	210	UV Light	92.7% MB	0.0169	This Study
Quasispherical ZnO nanoparticles	Coprecipitation	60	UV Light	67.78% MB	0.0197	[55]
ZnO nanoparticles	Flame spray pyrolysis	60	UV Light	~70% MB	0.0055	[56]
ZnO nanoparticles	Precipitation	180	UV Light	81.02% MB	0.0084	[57]
ZnO nanoparticles	Sol-gel	180	UV Light	92.48% MB	0.0124	[57]
ZnO nanoparticles	Precipitation	180	UV Light	6.6% MB	0.00015	[58]
ZnO nanoparticles	Biological synthesis	30	UV Light	38.08% MB	0.3594	[59]
ZnO nanoparticles	Coprecipitation	360	UV Light	79% MB	0.0032	[60]
ZnO nanorods	Sonarchemical	300	UV Light	~50% MB	0.00277	[61]
ZnO nano flower-like particles	Microwave-assisted sol–gel	60	UV Light	90% MB	0.0249	[62]
Au-ZnO nanocomposites	Green biomimetic approach	180	Visible Light	88% MB	0.0115	[63]
ZnO nanocubes	Pyrolysis	120	Visible Light	50% MB	0.00398	[64]
Sm doped ZnO thin film	Sol-gel spin coating	200	Sunlight	60% MB	0.00430	[65]
ZnO nanoparticles	Ball milled solventless process	150	Visible Light	~90% MB	0.0186	[66]
Au/ZnO/H_2O_2 catalytic system	Deposition–reduction method	120	Visible Light	–	0.0032	[67]
ZnO/70%CNT nanocomposites	Ultrasonication/hydrothermal	180	Visible light	98% MB	0.015	[68]
ZnO/Au10/Pd5 nanocomposites	Three–step pulsed laser ablation in liquid and photodeposition technique	180	Visible light	97% MB	0.0145	[69]
ZnO nanoparticles	Green synthesis approach	210	UV Light	98.6% MB	0.016	[70]
Ag doped ZnO nanoparticles	Combined sol-gel and chemical reduction	240	UV Light	81.2% MB	0.0068	[71]
ZnO nanoparticles	Conventional methodpeel extraction	120	UV Light	63% MB	0.00812	[72]
Cd doped ZnO nanorod film	Dip Coating	360	UV Light	–	0.00859	[73]
ZnO nanoparticles	One-step wet-chemical route	80	UV Light	32.68% MB	0.010	[74]

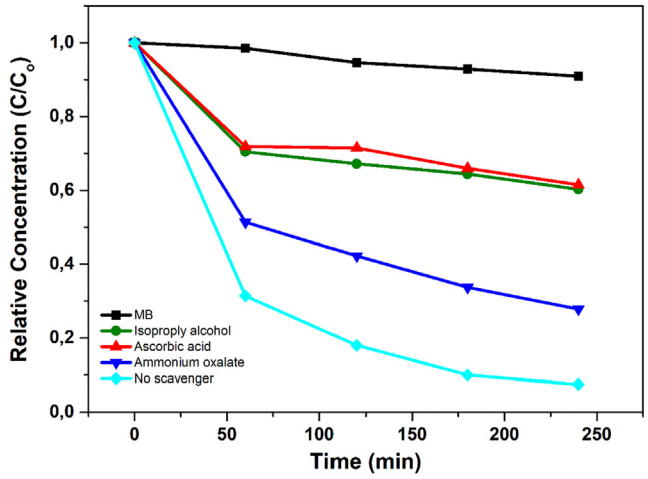

Fig. 11. Photocatalytic degradation of MB in the presence of different scavengers under light irradiation.

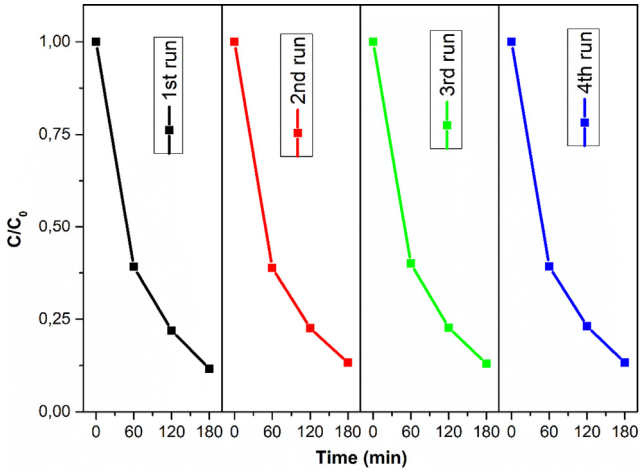

Fig. 12. Stability and reusability study of ZnO photocatalyst powders in the MB degradation process under irradiation for four runs.

As can be seen above photocatalytic degradation mechanism, the photocatalytic mechanism basically consist of four steps. The first step is light absorption. The second step is separation of photogenerated charge carriers. The third one is transfer carriers to surface of the catalyst. The last one is to react with redox reaction with the adsorbed reactants, respectively [77]. The ZnO synthesized at 1 °C/min heating rate photocatalysts were used to evaluate the reusability test for MB dye solution with multiple cycles in order to confirm the stability of the photocatalysts as shown in Fig. 12. After recycling four times, there were no significant changes in the degradation efficiency. This clearly indicates that the synthesized ZnO photocatalyst samples are reusable and stable enough for industrial and environmental applications. Photoluminescence analysis is a good technique in order to figure out, understand and verify the charge carrier trapping, migration and transfer. The PL emission spectrum is the result of recombination rate of electron-hole pairs generated by light irradiation. The ZnO samples exhibited emission peak center at ~506 nm when they are subjected to excitation at 372 nm as can be seen in Fig. 13(a). The existence of intense emission spectrum implies the rapid recombination rate of photogenerated electron-hole pairs [78–81]. The emission spectrum intensity of the particles became higher as the heating rate increased. The ZnO particles prepared at ∞ °C/min heating rate showed the highest intensity in emission spectra which means recombination of the photogenerated electron-hole pairs was very fast. Having a fast recombination influences the photocatalytic performances inversely. The fast recombination for ZnO particles prepared at ∞ °C/min heating rate could attributed to more surface defects such as oxygen vacancies [56]. The PL emission spectra of ZnO particles are supported by photocatalytic results. In addition to PL emission, decay time curves of ZnO powders are also measured. Lifetime of electrons and holes are very important for the photocatalytic application. The decay time profile provides an understanding of how long the photogenerated free carrier charges will recombine each other which is called lifetime of the charges [82,83]. The decay time profiles of the ZnO powders are given in Fig. 13(b). It was clearly seen that the ZnO powders prepared at 1 °C/min heating rate had slow decay time curve. There was a decline in

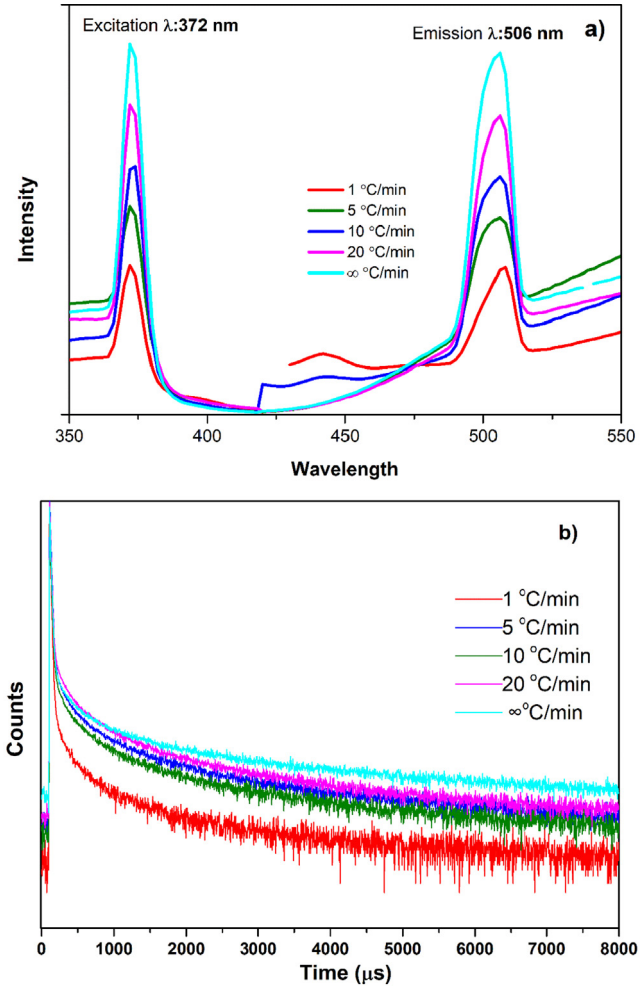

Fig. 13. Emission spectra (a) and decay curves (b) of ZnO samples synthesized at different heating rates.

decay time curves with increasing heating rate which indicates that recombination is becoming faster.

4. Conclusion

As a conclusion, pure ZnO particles were successfully fabricated by sol–gel method with different heating rate regime at 500 °C for 2 h. XRD patterns revealed that all ZnO samples had high degree of crystallinity. The heating rate didn't change the morphology of the ZnO powders which possessed almost same morphologies. Thermodynamic properties of the ZnO particles are calculated. The band gap of the ZnO particles prepared at 1 °C/min heating rate was 3.10 eV. The pure ZnO particles prepared at 1 °C/min heating rate had high surface oxygen vacancies based on Raman spectrum. The photocatalytic degradation efficiency of MB by ZnO particles dropped with increasing heating rate. ZnO sample prepared at 1 °C/min heating rate demonstrated the best photocatalytic properties. The photodegradation rate of MB solution was 92.7% and 1.069×10^{-2} min^{-1} kinetic constant value, respectively. Moreover, the ZnO particles showed good stability after four consecutive experiments. The heating rate regime should be a good way to enhance photocatalytic properties for photocatalytic materials.

CRediT authorship contribution statement

Selim Demirci: Conceptualization, Methodology, Data curation, Formal analysis, Funding acquisition, Writing - original draft, Writing - review & editing. **Tuncay Dikici:** Resources, Investigation, Supervision, Validation, Visualization. **Mehmet Masum Tünçay:** Formal analysis, Visualization, Writing - review & editing. **Nusret Kaya:** Software, Supervision, Validation, Visualization, Writing - review & editing.

Declaration of Competing Interest

The authors declare that they have no known competing financial interests or personal relationships that could have appeared to influence the work reported in this paper.

Acknowledgements

This work is supported by the Marmara University, Dokuz Eylül University and Katip Çelebi University, Central Research Laboratories Application and Research Center.

References

[1] T. Xu, et al., Significantly enhanced photocatalytic performance of ZnO via graphene hybridization and the mechanism study, Appl. Catal. B 101 (3) (2011) 382–387.
[2] C. Yang, et al., Synthesis, photocatalytic activity, and photogenerated hydroxyl radicals of monodisperse colloidal ZnO nanospheres, Appl. Surf. Sci. 357 (2015) 1928–1938.
[3] M. Samadi, et al., Recent progress on doped ZnO nanostructures for visible-light photocatalysis, Thin Solid Films 605 (2016) 2–19.
[4] I.K. Konstantinou, T.A. Albanis, TiO2-assisted photocatalytic degradation of azo dyes in aqueous solution: kinetic and mechanistic investigations: A review, Appl. Catal. B 49 (1) (2004) 1–14.
[5] S. Ahmed, et al., Influence of parameters on the heterogeneous photocatalytic degradation of pesticides and phenolic contaminants in wastewater: A short review, J. Environ. Manage. 92 (3) (2011) 311–330.
[6] X. Chen, et al., Preparation of ZnO photocatalyst for the efficient and rapid photocatalytic degradation of Azo dyes, Nanoscale Res. Lett. 12 (1) (2017) 143.
[7] U. Alam, et al., Highly efficient Y and V co-doped ZnO photocatalyst with enhanced dye sensitized visible light photocatalytic activity, Catal. Today 284 (2017) 169–178.
[8] P. Singh, A. Borthakur, A review on biodegradation and photocatalytic degradation of organic pollutants: A bibliometric and comparative analysis, J. Clean. Prod. 196 (2018) 1669–1680.
[9] R. Bomila, S. Suresh, S. Srinivasan, Synthesis, characterization and comparative studies of dual doped ZnO nanoparticles for photocatalytic applications, J. Mater. Sci.: Mater. Electron. 30 (1) (2019) 582–592.
[10] H.H. Mohamed, et al., Highly efficient Cu-phthalocyanine-sensitized ZnO hollow spheres for photocatalytic and antimicrobial applications, Compos. B Eng. 176 (2019) 107314.
[11] T. Tangcharoen, W. Klysubun, C. Kongmark, Synthesis of nanocrystalline NiO/ZnO heterostructured composite powders by sol-gel auto combustion method and their characterizations, J. Mol. Struct. 1156 (2018) 524–533.
[12] S. Wang, et al., ZnO hierarchical microsphere for enhanced photocatalytic activity, J. Alloy. Compd. 741 (2018) 622–632.
[13] T. Dikici, S. Demirci, Influence of thermal oxidation temperature on the microstructure and photoelectrochemical properties of ZnO nanostructures fabricated on the zinc scraps, J. Alloy. Compd. 779 (2019) 752–761.
[14] N.G. Shimpi, et al., Synthesis of ZnO nanopencils using wet chemical method and its investigation as LPG sensor, Appl. Surf. Sci. 390 (2016) 17–24.
[15] R.E. Adam, et al., Synthesis of ZnO nanoparticles by co-precipitation method for solar driven photodegradation of Congo red dye at different pH, Photon. Nanostruct. Fundam. Appl. 32 (2018) 11–18.
[16] D. Li, H. Haneda, Morphologies of zinc oxide particles and their effects on photocatalysis, Chemosphere 51 (2) (2003) 129–137.
[17] S. Baruah, J. Dutta, Hydrothermal growth of ZnO nanostructures, Sci. Technol. Adv. Mater. 10 (1) (2009) 013001.
[18] J.N. Hasnidawani, et al., Synthesis of ZnO Nanostructures Using Sol-Gel Method, Procedia Chem. 19 (2016) 211–216.
[19] R.V. Ramani, et al., Cr–ZnO nanostructured thin film coating on borosilicate glass by cost effective sol–gel dip coating method, Ain Shams Eng. J. 9 (4) (2018) 777–782.
[20] E.J. Luna-Arredondo, et al., Indium-doped ZnO thin films deposited by the sol–gel technique, Thin Solid Films 490 (2) (2005) 132–136.
[21] N.R.S. Farley, et al., Sol-gel formation of ordered nanostructured doped ZnO films, J. Mater. Chem. 14 (7) (2004) 1087–1092.
[22] E. Kilinc, et al., High temperature thermopower of sol–gel processed Zn1−x−yAlxMeyO (Me: Ga, In), J. Mater. Sci.: Mater. Electron. 28 (16) (2017) 11769–11778.
[23] R. Mahdavi, S.S. Ashraf Talesh, The effect of ultrasonic irradiation on the structure, morphology and photocatalytic performance of ZnO nanoparticles by sol-gel method, Ultrason. Sonochem. 39 (2017) 504–510.
[24] L.W. Wang, et al., Effects of Na content on structural and optical properties of Na-doped ZnO thin films prepared by sol–gel method, J. Alloy. Compd. 623 (2015)

367–373.
[25] S. Rani, et al., Synthesis of nanocrystalline ZnO powder via sol–gel route for dye-sensitized solar cells, Sol. Energy Mater. Sol. Cells 92 (12) (2008) 1639–1645.
[26] M.M. Ba-Abbad, et al., The effect of process parameters on the size of ZnO nanoparticles synthesized via the sol–gel technique, J. Alloy. Compd. 550 (2013) 63–70.
[27] M. Gao, et al., The effect of heating rate on the structural and electrical properties of sol–gel derived Al-doped ZnO films, Appl. Surf. Sci. 257 (15) (2011) 6919–6922.
[28] L. He, et al., Effects of calcination temperature and heating rate on the photocatalytic properties of ZnO prepared by pyrolysis, J. Colloid Interface Sci. 509 (2018) 448–456.
[29] P. Kanmani, J.-W. Rhim, Properties and characterization of bionanocomposite films prepared with various biopolymers and ZnO nanoparticles, Carbohydr. Polym. 106 (2014) 190–199.
[30] M.M. Ba-Abbad, et al., Visible light photocatalytic activity of Fe3+-doped ZnO nanoparticle prepared via sol–gel technique, Chemosphere 91 (11) (2013) 1604–1611.
[31] Ö. Çepelioğullar, H. Haykırı-Açma, S. Yaman, Kinetic modelling of RDF pyrolysis: Model-fitting and model-free approaches, Waste Manage. 48 (2016) 275–284.
[32] J.H. Flynn, L.A. Wall, General treatment of the thermogravimetry of polymers, J. Res. Natl. Bureau Standards Section A Phys. Chem. 70A (6) (1966) 487.
[33] O. Takeo, A new method of analyzing thermogravimetric data, Bull. Chem. Soc. Jpn. 38 (11) (1965) 1881–1886.
[34] M.J. Starink, The determination of activation energy from linear heating rate experiments: a comparison of the accuracy of isoconversion methods, Thermochim. Acta 404 (1) (2003) 163–176.
[35] A. Mahmood, F. Tezcan, G. Kardaş, Thermal decomposition of sol-gel derived Zn0.8Ga0.2O precursor-gel: A kinetic, thermodynamic, and DFT studies, Acta Mater. 146 (2018) 152–159.
[36] B. Lallo da Silva, et al., Increased antibacterial activity of ZnO nanoparticles: Influence of size and surface modification, Colloids Surf., B 177 (2019) 440–447.
[37] V. Srivastava, D. Gusain, Y.C. Sharma, Synthesis, characterization and application of zinc oxide nanoparticles (n-ZnO), Ceram. Int. 39 (8) (2013) 9803–9808.
[38] S. Aksoy, et al., Sol–gel derived Li–Mg co-doped ZnO films: Preparation and characterization via XRD, XPS, FESEM, J. Alloys Compound. 512 (1) (2012) 171–178.
[39] I.N. Reddy, et al., Effect of ball milling on optical properties and visible photocatalytic activity of Fe doped ZnO nanoparticles, Mater. Sci. Eng., B 240 (2019) 33–40.
[40] F.C. Correia, et al., XPS analysis of ZnO: Ga films deposited by magnetron sputtering: Substrate bias effect, Appl. Surf. Sci. 458 (2018) 1043–1049.
[41] S. Wang, et al., Controllable fabrication of homogeneous ZnO p-n junction with enhanced charge separation for efficient photocatalysis, Catal. Today 335 (2019) 151–159.
[42] R. Zhang, et al., Photoluminescence and Raman scattering of ZnO nanorods, Solid State Sci. 11 (4) (2009) 865–869.
[43] J. Das, et al., Micro-Raman and XPS studies of pure ZnO ceramics, Physica B 405 (10) (2010) 2492–2497.
[44] A.R. Landa-Cánovas, et al., Nanostructural changes upon substitutional Al doping in ZnO sputtered films, Ceram. Int. 45 (5) (2019) 6319–6327.
[45] N. Salah, et al., Size controlled, antimicrobial ZnO nanostructures produced by the microwave assisted route, Mater. Sci. Eng., C 99 (2019) 1164–1173.
[46] J. Wang, et al., Defect-rich ZnO nanosheets of high surface area as an efficient visible-light photocatalyst, Appl. Catal. B 192 (2016) 8–16.
[47] M. Šćepanović, et al., Raman study of structural disorder in ZnO nanopowders, J. Raman Spectrosc. 41 (9) (2010) 914–921.
[48] L.V. Trandafilović, et al., Enhanced photocatalytic degradation of methylene blue and methyl orange by ZnO: Eu nanoparticles, Appl. Catal. B 203 (2017) 740–752.
[49] C. Wang, et al., Effect of oxygen vacancy on enhanced photocatalytic activity of reduced ZnO nanorod arrays, Appl. Surf. Sci. 325 (2015) 112–116.
[50] M.Y. Guo, et al., Effect of native defects on photocatalytic properties of ZnO, J. Phys. Chem. C 115 (22) (2011) 11095–11101.
[51] J. Wang, et al., Synthesis, properties and applications of ZnO nanomaterials with oxygen vacancies: A review, Ceram. Int. 44 (7) (2018) 7357–7377.
[52] D. Chen, et al., Influence of defects on the photocatalytic activity of ZnO, J. Phys. Chem. C 118 (28) (2014) 15300–15307.
[53] Y. Li, et al., Comparison of dye photodegradation and its coupling with light-to-electricity conversion over TiO2 and ZnO, Langmuir 26 (1) (2010) 591–597.
[54] D. Chaudhary, et al., ZnO nanoparticles decorated multi-walled carbon nanotubes for enhanced photocatalytic and photoelectrochemical water splitting, J. Photochem. Photobiol., A 351 (2018) 154–161.
[55] J. Lin, et al., Photocatalytic degradation of methylene blue in aqueous solution by using ZnO-SnO2 nanocomposites, Mater. Sci. Semicond. Process. 87 (2018) 24–31.
[56] O. Mekasuwandumrong, et al., Effects of synthesis conditions and annealing post-treatment on the photocatalytic activities of ZnO nanoparticles in the degradation of methylene blue dye, Chem. Eng. J. 164 (1) (2010) 77–84.
[57] A. Balcha, O.P. Yadav, T. Dey, Photocatalytic degradation of methylene blue dye by zinc oxide nanoparticles obtained from precipitation and sol-gel methods, Environ. Sci. Pollut. Res. 23 (24) (2016) 25485–25493.
[58] R. Saravanan, et al., Conducting PANI stimulated ZnO system for visible light photocatalytic degradation of coloured dyes, J. Mol. Liq. 221 (2016) 1029–1033.
[59] N. Jain, A. Bhargava, J. Panwar, Enhanced photocatalytic degradation of methylene blue using biologically synthesized “protein-capped” ZnO nanoparticles, Chem. Eng. J. 243 (2014) 549–555.
[60] R. Rameshbabu, et al., Visible light photocatalytic activities of ZnFe2O4/ZnO nanoparticles for the degradation of organic pollutants, Mater. Chem. Phys. 181 (2016) 106–115.
[61] O. Yayapao, et al., Synthesis and characterization of highly efficient Gd doped ZnO photocatalyst irradiated with ultraviolet and visible radiations, Mater. Sci. Semicond. Process. 39 (2015) 786–792.
[62] H. Parangusan, et al., Nanoflower-like Yttrium-doped ZnO Photocatalyst for the Degradation of Methylene Blue Dye, Photochem. Photobiol. 94 (2) (2018) 237–246.
[63] M.K. Choudhary, J. Kataria, S. Sharma, Novel green biomimetic approach for preparation of highly stable Au-ZnO heterojunctions with enhanced photocatalytic activity, ACS Appl. Nano Mater. 1 (4) (2018) 1870–1878.
[64] S. Payra, et al., Probing the photo- and electro-catalytic degradation mechanism of methylene blue dye over ZIF-derived ZnO, J. Hazard. Mater. 373 (2019) 377–388.
[65] D. Ali, et al., Synthesis and characterization of sol-gel derived La and Sm doped ZnO thin films: A solar light photo catalyst for methylene blue, Thin Solid Films 679 (2019) 86–98.
[66] S.P. Lonkar, V. Pillai, A. Abdala, Solvent-free synthesis of ZnO-graphene nanocomposite with superior photocatalytic activity, Appl. Surf. Sci. 465 (2019) 1107–1113.
[67] L. Wolski, A. Walkowiak, M. Ziolek, Formation of reactive oxygen species upon interaction of Au/ZnO with H2O2 and their activity in methylene blue degradation, Catal. Today 333 (2019) 54–62.
[68] M.M. Mohamed, et al., Zinc oxide incorporated carbon nanotubes or graphene oxide nanohybrids for enhanced sonophotocatalytic degradation of methylene blue dye, Appl. Surf. Sci. 487 (2019) 539–549.
[69] S.J. Lee, et al., ZnO supported Au/Pd bimetallic nanocomposites for plasmon improved photocatalytic activity for methylene blue degradation under visible light irradiation, Appl. Surf. Sci. 496 (2019) 143665.
[70] L. Chen, et al., Green synthesis of zinc oxide nanoparticles from root extract of Scutellaria baicalensis and its photocatalytic degradation activity using methylene blue, Optik 184 (2019) 324–329.
[71] M.F. Abdel Messih, et al., Synthesis and characterization of novel Ag/ZnO nanoparticles for photocatalytic degradation of methylene blue under UV and solar irradiation, J. Phys. Chem. Solids 135 (2019) 109086.
[72] G. Madhumitha, et al., Green synthesis, characterization and antifungal and photocatalytic activity of Pithecellobium dulce peel–mediated ZnO nanoparticles, J. Phys. Chem. Solids 127 (2019) 43–51.
[73] S. Tian, et al., Mesoporous ZnO nanorods array with a controllable area density for enhanced photocatalytic properties, J. Colloid Interface Sci. 534 (2019) 389–398.
[74] Q. Sun, et al., Facile synthesis of zinc oxide crystal and insight into its morphological effect on organic dye photodegradation in water, Appl. Nanosci. 9 (1) (2019) 93–103.
[75] T. Liu, et al., Comparative study of the photocatalytic performance for the degradation of different dyes by ZnIn2S4: adsorption, active species, and pathways, RSC Adv. 7 (20) (2017) 12292–12300.
[76] K. Das, A. Roychoudhury, Reactive oxygen species (ROS) and response of antioxidants as ROS-scavengers during environmental stress in plants, Front. Environ. Sci. 2 (53) (2014).
[77] R. Marschall, L. Wang, Non-metal doping of transition metal oxides for visible-light photocatalysis, Catal. Today 225 (2014) 111–135.
[78] Y. Cao, et al., Mesoporous black TiO2-x/Ag nanospheres coupled with g-C3N4 nanosheets as 3D/2D ternary heterojunctions visible light photocatalysts, J. Hazard. Mater. 343 (2018) 181–190.
[79] A.A. Othman, et al., Mn-doped ZnO nanocrystals synthesized by sonochemical method: Structural, photoluminescence, and magnetic properties, Mater. Sci. Eng., B 219 (2017) 1–9.
[80] S. Demirci, et al., Fabrication and characterization of novel iodine doped hollow and mesoporous hematite (Fe2O3) particles derived from sol-gel method and their photocatalytic performances, J. Hazard. Mater. 345 (2018) 27–37.
[81] Haghshenas, S.S.P., et al., Photocatalytic and photoluminescence properties of ZnO/graphene quasi core-shell nanoparticles. Ceram. Int., (2019) 45(7, Part A) pp. 8945–8961.
[82] K. Fujihara, et al., Time-resolved photoluminescence of particulate TiO2 photocatalysts suspended in aqueous solutions, J. Photochem. Photobiol., A 132 (1) (2000) 99–104.
[83] Y. Yamada, Y. Kanemitsu, Determination of electron and hole lifetimes of rutile and anatase TiO2 single crystals, Appl. Phys. Lett. 101 (13) (2012) 133907.